Journal of Power Sources 213 (2012) 31–39

Contents lists available at SciVerse ScienceDirect

Journal of Power Sources

journal homepage: www.elsevier.com/locate/jpowsour

Electrochemical properties of pure $Ba_{0.5}Sr_{0.5}Co_{0.8}Fe_{0.2}O_3$ and $Ba_{0.5}Sr_{0.5}Co_{0.8}Fe_{0.2}O_3$-based composite cathodes for an intermediate temperature solid oxide fuel cell with Sc-doped zirconia solid electrolyte

Hee Jung Park*, Chan Kwak, Ju Sik Kim, Sung Jin Ahn

Samsung Advanced Institute of Technology (SAIT), 14-1 Nongseo-dong, Yongin-si 446-712, Republic of Korea

ARTICLE INFO

Article history:
Received 11 February 2012
Received in revised form
23 March 2012
Accepted 25 March 2012
Available online 19 April 2012

Keywords:
Solid oxide fuel cell
Composite cathode
Impedance spectroscopy
Cathodic polarization resistance

ABSTRACT

The electrochemical properties of $Ba_{0.5}Sr_{0.5}Co_{0.8}Fe_{0.2}O_3$, $Ba_{0.5}Sr_{0.5}Co_{0.8}Fe_{0.2}O_3 + Co_3O_4$, and $Ba_{0.5}Sr_{0.5}Co_{0.8}Fe_{0.2}O_3 + Co_3O_4 + Ce_{0.8}Sm_{0.15}Nd_{0.05}O_2$ as cathode materials on a zirconia solid electrolyte with a ceria buffer layer have been investigated. Impedance spectra are measured to investigate theircathodic polarization resistances in cells in a symmetric configuration. The $Ba_{0.5}Sr_{0.5}Co_{0.8}Fe_{0.2}O_3 + Co_3O_4 + Ce_{0.8}Sm_{0.15}Nd_{0.05}O_2$ composite shows extremely low polarization resistance of 0.048 $\Omega\,cm^2$ at 700 °C, which is an improved value over the $Ba_{0.5}Sr_{0.5}Co_{0.8}Fe_{0.2}O_3$ due to enhanced mixed ionic and electronic conductivity. This low polarization resistance is confirmed by conducting an electrochemical impedance spectroscopy analysis on a large tubular SOFC fabricated with the composite cathode. The tubular SOFC exhibits good cell performance of 0.400 $W\,cm^{-2}$ under 0.7 V and at 700 °C and stable performance for 280 h.

1. Introduction

Solid oxide fuel cells (SOFCs) are environmentally friendly highly efficient electrochemical power generation devices that directly convert chemical energy of a fuel gas into electrical energy. SOFCs use relatively inexpensive materials compared to other types of fuel cells and have relatively high tolerance to fuel impurities, while offering hybrid power generation capability and high efficiency [1–4]. Conventional SOFCs, however, operate at very high temperature (>700 °C), leading to chemical/mechanical instability and high operation cost. It is generally believed that reduction of operation temperature from higher than 700 °C to an intermediate temperature range of 550–700 °C is a possible solution for the commercialization of SOFCs [5–7]. The intermediate temperature (IT) would not only reduce the operation cost but also effectively increase the durability of the fuel cells by suppressing the interfacial reaction of cell components and particle growths of electrode materials. However, the reduction in operation temperature requires enhanced electrochemical reaction kinetics in the cathode.

Sr-doped $LaMnO_3$ (LSM) has been conventionally used as a cathode material for SOFCs because of its high electrochemical properties for oxygen reduction and good stability and compatibility with zirconia solid electrolyte (SE) [8–10]. However, it is unsuitable for the cathode of IT-SOFCs due to inadequate electrochemical performance at low temperatures resulting from deteriorated oxygen ionic conductivity [10]. Extensive efforts have thus been directed toward finding novel cathode materials with high mixed ionic and electronic conductivity, which would extend the three-phase boundary (TPB) at which oxygen reduction reaction takes place. Perovskites containing cobalt or iron such as $Ba_{0.5}Sr_{0.5}Co_{0.8}Fe_{0.2}O_3$ (BSCF), $Sm_{0.5}Sr_{0.5}CoO_3$ (SSC), and $La_{0.6}Sr_{0.4}Co_{0.2}Fe_{0.8}O_3$ (LSCF), instead of Mn as a B-site atom of perovskite (ABO_3), have been identified as candidates [5,6,11–15].

Among them, BSCF was initially developed by Shao et al. as a good ceramic oxygen-separation membrane material [16]. The oxygen permeability of a mixed conducting membrane is closely related to the electronic and oxygen ionic conductivity of the membrane material, thus implying that BSCF is potentially a good cathode material. Shao and Haile first investigated the electrochemical performance of BSCF as an IT-SOFC cathode and demonstrated excellent low-temperature electrode performance [5]. A thin samaria-doped ceria (SDC) electrolyte film (thickness: 20 μm) single SOFC-cell with a BSCF cathode was fabricated and the maximum power output of the cell was ~1010 mW cm^{-2} at 600 °C. This attractive performance in terms of electrode polarization resistance was obtained under contact with a doped ceria electrolyte; however, BSCF shows high reactivity with the stabilized-zirconia electrolyte, leading to greatly reduced cell performance and fuel cell durability (It should be noted that insulating

* Corresponding author. Tel.: +82 31 280 8353; fax: +82 31 280 6739.
E-mail address: hj2007.park@samsung.com (H.J. Park).

0378-7753/$ – see front matter © 2012 Elsevier B.V. All rights reserved.
doi:10.1016/j.jpowsour.2012.03.093

phases ($SrZrO_3$ or $BaZrO_3$) between the cathode and electrolyte interface are formed). A doped ceria buffer layer is applied often to prevent the formation of insulating phases between them [5,14,17–19]. BSCF also has a high thermal expansion coefficient (TEC: $19.2–22.9 \times 10^{-6}\,K^{-1}$ between 25 °C and 850 °C), much higher than that of stabilized-zirconia electrolyte, as well as large chemical expansion coefficient, and a low melting point (1180 °C) [20–22]. For a reliable cathode material, in addition to electronic/catalytic functionality, similar (or preferably identical) thermal expansion of the cathode with the electrolyte and high melting temperature are prerequisites. The mismatch in thermal expansion of the cathode and electrolyte could result in delamination of the cathode layer from the electrolyte surface, and thus poor durability of the fuel cell. High melting temperature of the cathode is also required in order to prevent coarsening of cathode particles.

It has been found that composite cathodes often offer better cell performance and durability than single-phase cathodes [23]. Introducing solid electrolyte materials with high ionic conductivity and melting point into the cathode materials provides for an extended TPB and durability, leading to enhanced cathodic performance. It has also been reported that composite cathodes often reduce the thermal expansion coefficient mismatch between the cathode and electrolyte and enhance adhesion between them [24,25].

We present here a novel BSCF composite cathode ($0.72BSCF + 0.08Co_3O_4 + 0.20\,Ce_{0.8}Sm_{0.15}Nd_{0.05}O_2$ (SNDC)) for application to IT-SOFCs. Co_3O_4 and SNDC were added to BSCF because the cobaltate has high electronic conductivity and the ceria high ionic conductivity. Further, the ceria has a lower TEC and higher melting point than BSCF. For comparison, pure BSCF and BSCF + Co_3O_4 cathodes also have been studied.

2. Experimental

To obtain the BSCF–Co_3O_4–SNDC composite (BCS) cathode material, the solid reaction method was used. BSCF, Co_3O_4, and SNDC (0.72:0.08:0.20 wt. ratio) were mixed in ethyl alcohol and then ball-milled with zirconia balls for 12 h. The composite powders were obtained after drying on a hot plate (80 °C) with stirring. The BSCF + Co_3O_4 (BC) composite was obtained in the same manner. The used BSCF (BSCF5582, Kceracell Co., Ltd, Korea) and Co_3O_4 (Alfa, 99.7%, USA) powders were commercial products. SNDC was synthesized based on the solid state reaction method. Appropriate amounts of CeO_2 (Alfa, 99.9%, USA), Sm_2O_3 (Aldrich 99.99%, USA), and Nd_2O_3 (Alfa, 99.5%, USA) were mixed in ethyl alcohol and then ball-milled with zirconia balls for 12 h. The slurry was dried on a hot plate with stirring followed by high temperature calcination (1200 °C for 2 h). The calcined powders were sieved 2 times through a 75-μm mesh sieve.

The average particle size and particle distribution of BSCF, Co_3O_4, and SNDC were assessed via a PSA (particle size analysis, HORIBA LA-910, Japan). The BCS powders fired at various temperatures (800–1000 °C) were characterized by using an X-ray diffractometer (XRD, X'pert, Philips). The scanning speed was 4° per min and the step size was 0.03°. The microstructures of the cathodes were examined using a field emission scanning electron microscope (FE-SEM, S-4700, Hitachi). The accelerating voltage was 15 kV and a secondary electron detector was used as a detector.

To measure the electrical conductivities of BSCF, BC, and SNDC, dense bulk samples were prepared. The BSCF and BC powders were pressed into pellets using a stainless steel mold and sintered at 1100 °C for 5 h in air. For the SNDC bulk sample, the calcined ceria powders were pressed into pellets followed by cold isostatic pressing (CIP) at 200 MPa. The pressed pellets were sintered at 1550 °C for 10 h in air. The relative densities of all sintered samples were higher than 90%. Their electrical conductivities were measured using the 4-probe dc technique. Rectangular bar-shaped samples were cut from the sintered pellets and Pt paste (Engelhard model #6926) electrodes were painted at four notches. Direct current was supplied to the samples and the corresponding voltage drop was measured by a current–voltage sourcemeter (Keithley, 2400).

The cathodic polarization resistances of the cathodes were checked using the 2-probe ac impedance technique with symmetric cells. The cell configuration with the BCS cathode (BCS_cell) was BCS |GDC (buffer layer)| ScSZ (solid electrolyte) |GDC (buffer layer)| BCS. To fabricate the symmetric cell, ScSZ ($Zr_{0.8}Sc_{0.2}O_2$, FCM) powders were pressed into a pellet and then sintered at 1550 °C for 8 h in air. The diameter and thickness of the sintered pellet were 1.2 cm and 0.1 cm, respectively. GDC ($Ce_{0.9}Gd_{0.1}O_2$, BET: 11.8 $m^2\,g^{-1}$, FCM, USA) powders for the buffer layer were then screen-printed on both surfaces of the zirconia electrolyte and thermally treated at 1400 °C for 2 h in air. The BCS cathode was subsequently screen-printed on the buffer layer followed by firing. In order to determine the optimal firing temperature, five cells were fabricated with different firing temperatures from 800 to 1000 °C with a step of 50 °C. The cathode active area was 0.78 cm^2. Other cells with different cathodes (BSCF or BC) were also fabricated. Their cathode firing temperatures were 900 °C.

The cathodic polarization resistances were investigated by Electrochemical Impedance Spectra (EIS) measurements using an impedance analyzer (Materials Mates 7260, Italy) after electroding with an Ag-paste (H4580, Shoei chemical, Japan). The obtained EIS data were analyzed using Z-view software (Scribner associates) to estimate the resistance (R) of the sample. The EIS tests were conducted as a function of temperature (500–700 °C) and oxygen partial pressure (PO_2 : 1–0.0066 atm). Ac impedance spectra were obtained in a frequency range of 0.1–10 MHz at an amplitude of 50 mV.

In order to verify the electrochemical performances of the cathodes, anode-support type tubular SOFCs with large active area (34.5 cm^2) were constructed. The diameter of the tubular cells is 2.2 cm and cathode-coated length is 5 cm. The cell configuration of the tubular cell was cathode |GDC (buffer layer)| ScSZ (solid electrolyte) |AFL| NiO-YSZ anode, where AFL denotes the anode functional layer and YSZ ($Zr_{0.84}Y_{0.16}O_{2-\delta}$) yttria stabilized zirconia. For the construction of the tubular cell, a commercial anode support (Khancera, Korea) composed of NiO and YSZ was used. The AFL layer with submicron-sized NiO (Sumitomo, Japan) and nano-sized ScSZ (FCM, USA) was first coated on the surface of the anode support using a dip-coating technique and then fired at 900 °C for 2 h. A slurry for the solid electrolyte was fabricated using butyl alcohol media and coated on top of the AFL layer in the same manner followed by firing at 1350 °C for 5 h. Finally, the cathode was dip-coated and fired at 900 °C for 2 h after constructing the GDC buffer layer.

The current–voltage characteristics were evaluated and EIS tests of the tubular cell were carried out as a function of temperature (650–800 °C) using an electronic loader (Wonatech, Korea). For the electrochemical tests, Ag-mesh and wire (Alfa, USA) were wound on the surface of the cathode and Ni-felt (SMDC, Korea) was put into anode side as current collection. The impedance spectra were obtained by an electric loader and FRA (Wonatech, Z100, Korea) over a frequency range of 0.1 Hz to 10 kHz with ac amplitude of 0.5 V under a 0.8 V operation condition.

3. Results and discussion

3.1. X-ray diffraction

The BCS composites obtained using a ball-milling process with zirconia grinding balls and ethanol were calcined at various temperatures and characterized by XRD to investigate the reaction between

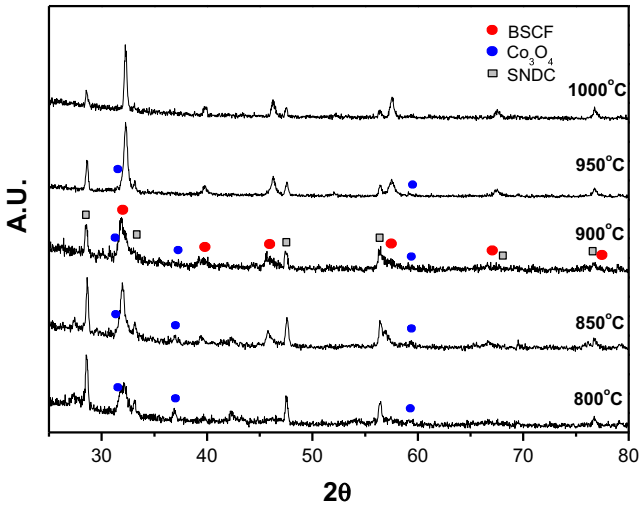

Fig. 1. X-ray diffraction patterns of BCS fired at 800 °C, 850 °C, 900 °C, 950 °C, and 1000 °C, respectively.

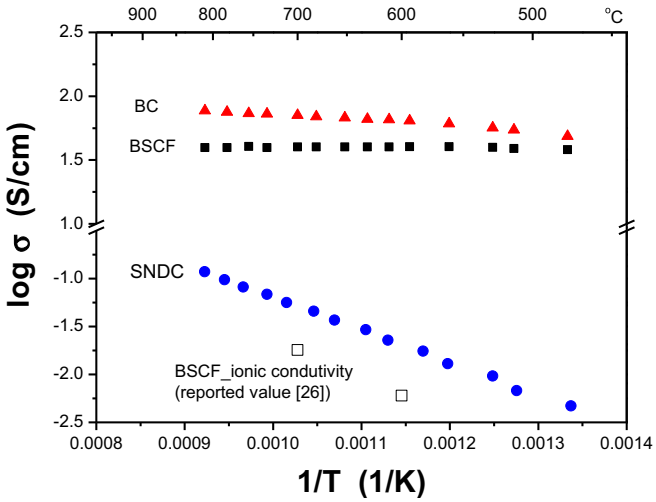

Fig. 3. Electrical properties of BSCF, BC, and SNDC as a function of temperature. The reported value indicates the oxygen ionic conductivity of BSCF ($Ba_{0.5}Sr_{0.5}Co_{0.8}Fe_{0.2}O_3$).

BSCF, Co_3O_4, and SNDC. Fig. 1 shows the X-ray diffraction patterns of the BCS calcined from 800 °C to 1000 °C with a step of 50 °C. The patterns were indexed based on a physical mixture of the BSCF phase with cubic perovskite, the Co_3O_4 phase with a spinel structure, and SNDC with a cubic fluorite structure below 900 °C (close, open, and window circles in this figure indicate BSCF, Co_3O_4, and SNDC, respectively). However, the cobaltate was no longer detected at 1000 °C firing, implying that it may react with other phases.

3.2. Microstructures

Three types of symmetric cells with BSCF, BC, and BCS were fabricated. Fig. 2(a) shows the microstructure of the BCS_cell (BCS |GDC (buffer layer)| ScSZ (solid electrolyte) |GDC (buffer layer)| BCS). Fig. 2(b)–(f) shows the BCS layers of BCS_cells fired at 800–1000 °C, respectively (the numbers indicate the cathode firing temperatures). Good adhesion between each layer is achieved and the components (BSCF, Co_3O_4, and SNDC) are randomly distributed as indicated in Fig. 2(b). The components are estimated from the results of EDS and PSA (the average particle sizes of BSCF, Co_3O_4, and SNDC measured by PSA are ~0.62 μm, ~3.15 μm, and ~0.55 μm, respectively). The average particle size of BCS increases with temperature.

3.3. Electrical properties

Fig. 3 shows the electrical conductivities of BSCF, BC, and SNDC as a function of temperature, where the dominant charge carriers of

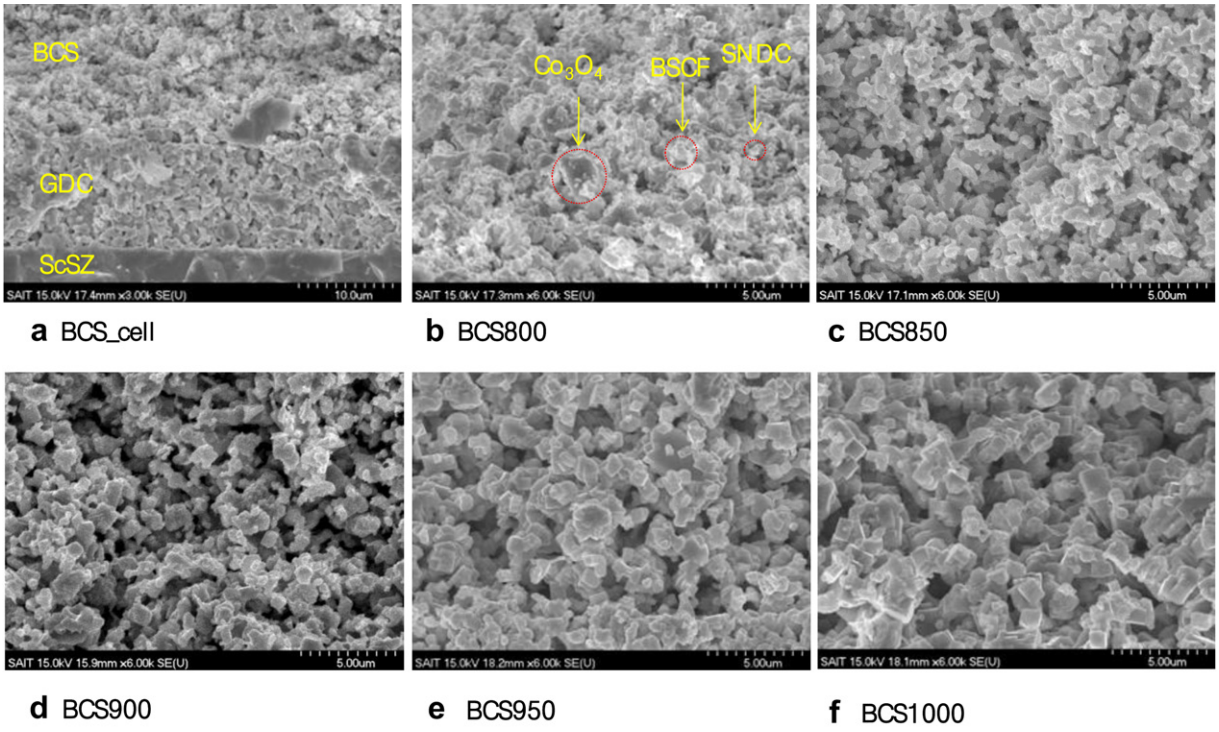

Fig. 2. SEM photographs of BCS_cell. (a) is the fractured surface of BCS_cell fired at 800 °C (cathodic firing temperature). (b)–(f) are the BCS layers of BC_cell fired 800 °C, 850 °C, 900 °C, 950 °C, and 1000 °C, respectively. Inserts in (b) indicate the representative particles of BSCF, Co_3O_4, and SNDC, respectively.

BSCF and BC are electrons while that of SNDC is a charged oxygen vacancy. The electrical conductivity of BSCF first steadily increased with temperature and then reached a level of approximately 40 S cm^{-1} at around 550 °C, while that of BC continuously increased with temperature. Within a temperature range of interest (600–800 °C), the electrical conductivity of BC is higher than that of BSCF.

SNDC shows very fast oxygen ionic conduction. The ionic conductivity of SNDC at 700 °C is higher (0.053 S cm^{-1}) than the value (0.018 S cm^{-1}) reported for BSCF (note that the reported conductivity of BSCF (in Fig. 3) is the oxygen ionic conductivity) [26]. As mentioned previously, the high mixed ionic and electronic conductivity extends the TPB of the cathode leading to high electrochemical performance. Thus, the cathodic resistance of BCS containing BSCF, Co_3O_4, and SNDC would be lower than that of pure BSCF. This is verified by the following EIS study.

3.4. EIS study

BSCF as a cathode material for IT-SOFCs has received much attention since being reported in *Nature* (2004). However, while a number of tests have been conducted on SOFC-systems using dense ceria SE [5,6], little attention has been paid to SOFC-systems with dense zirconia SE due to the mismatch of the TEC and a chemical reaction between the cathode and Zr-ions (note that the zirconia as a solid electrolyte is more widely used than ceria due to the mechanical and redox stabilities and material costs, and thus it is worth studying the electrochemical properties of BSCF on zirconia SE with a ceria buffer layer). Thus, in this study, prior to dealing with the BCS cathode, EIS tests for the BSCF cathode were first carried out.

Fig. 4(a) shows representative impedance spectra (i.e. Nyquist plot) of the BSCF_cell measured at 550 °C in $PO_2 \sim 0.05$ atm. The numbers indicate the measured frequency in a logarithmic scale. As indicated in the figure, the high-frequency offset is the ohmic resistance (R_{ohmic}) and the low-frequency offset is the cathodic polarization resistance (R_p) of the cell. It is known that R_{ohmic} is attributed to electrolyte resistance (R_{SE}), electrode ohmic resistance, current collection resistance, and contact resistance between the cathode and the SE. However, it was found that most of R_{ohmic} results from R_{SE} because the computed resistivity ($\rho_{ohmic} = R_{ohmic} \times A/L$, ~111 Ω cm at 550 °C, where A and L is area and thickness) is very close to the oxygen ionic resistivity of ScSZ at that temperature (we examined the ionic conductivity of ScSZ using 4-p dc measurement. ρ_{ScSZ} is ~119 Ω cm at 550 °C).

The impedance spectra related to R_p consist of three imperfect semicircular arcs, as seen in Fig. 4(a). Several depressed arcs are observed for the electrodes and may be attributed to multiple reactions involved in the polarization process. To determine each resistance, the impedance patterns were numerically fitted with R_{ohmic}-R_1Q_1-R_2Q_2-R_3Q_3 circuits in series (see the inserted schematic diagram in Fig. 4(a) where R and Q denote the resistance and constant phase element (Q = CPE), respectively. Q indicates the depression of a semicircular arc due to distribution of the relaxation time constant ($\tau = RC$) with C being the capacitance) [27]. The solid curved line indicates the best fit. From the fit, the resistances (R_1, R_2, and R_3) were computed.

Fig. 4(b) shows a Bode plot of BSCF_cell (real and imaginary impedance depending on frequency). The real impedance (Z_1)

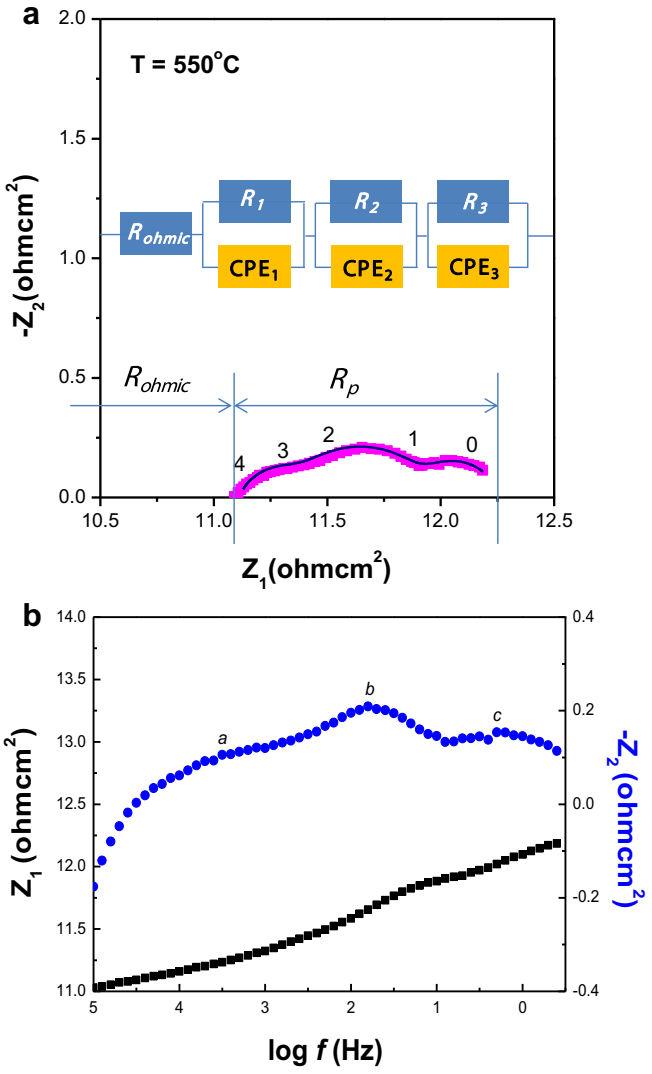

Fig. 4. (a) The impedance spectra of BSCF_cell at 550 °C. R_{ohmic} and R_p are the ohmic resistance and the polarization resistance of the cell, respectively. (b) Bode plot obtained from the cell.

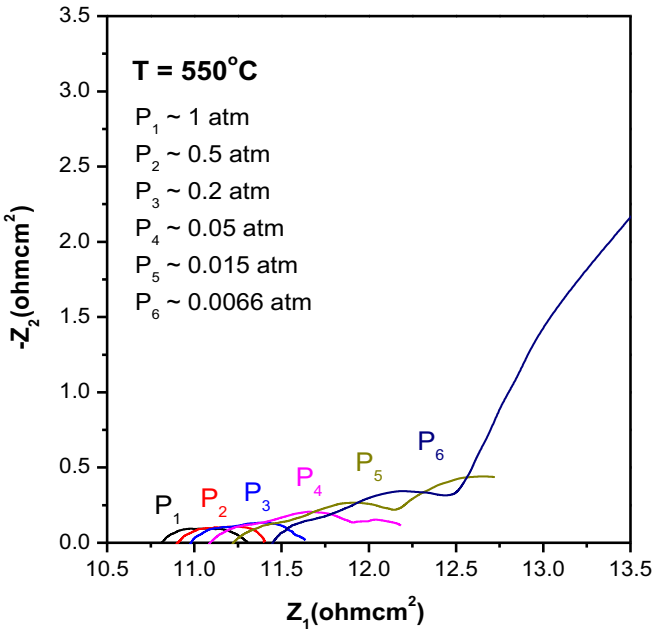

Fig. 5. Impedance spectra of BSCF_cell measured at different oxygen partial pressures.

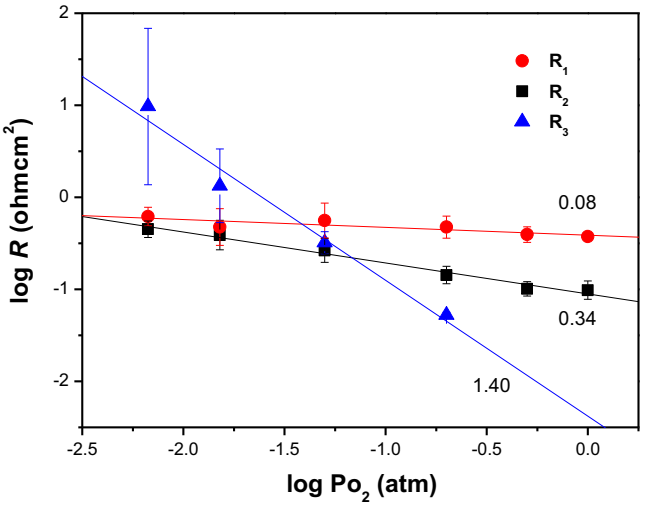

Fig. 6. Fitting values of R_p depending on PO_2.

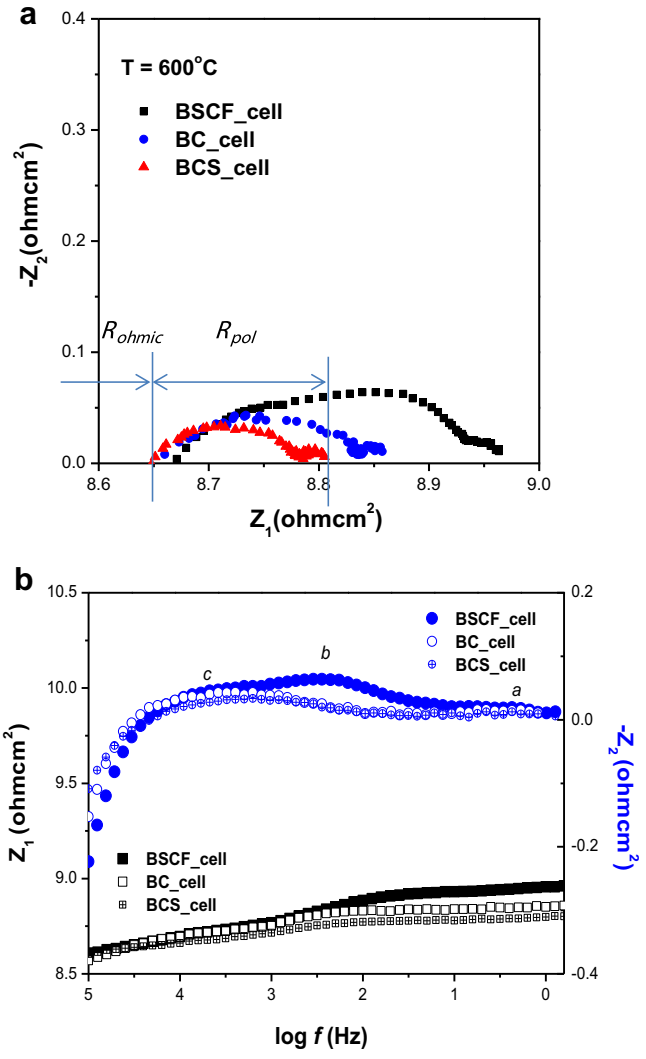

Fig. 7. (a) Impedance spectra of BSCF_cell, BC_cell, and BCS_cell measured at 600 °C in air. (b) Bode plots obtained from the cells.

increases with a decrease of the frequency. The imaginary impedance (Z_2) exhibits three peaks (a, b, and c in Fig. 4(b)). The summit frequency (f_{max}) is taken as the frequency at the measurement point having the maximum imaginary value. f_{max}s is 3981 Hz (*a*), 50 Hz (*b*), and 1.58 Hz (*c*). The several f_{max}s values reflect the existence of competitive elementary processes in the overall oxygen reduction reaction (ORR). According to an earlier report, the values of f_{max}s at *a* and *b* are related with dissociative adsorption, charge transfer, and surface diffusion [8]. f_{max} at low frequency (*c*) is closely linked to gas diffusion [8]. In order to identify the limiting elementary processes in the BSCF cathode, EIS tests were performed as a function of PO_2.

Fig. 5 shows the obtained impedance patterns at various PO_2 at 550 °C. The pattern size increases with a decrease of PO_2, indicating that R_p increases with decreasing PO_2. As done in Fig. 4(a), all patterns were numerically fitted to obtain each resistance. The PO_2 dependency of the obtained resistance is exhibited in Fig. 6. The value inserted in this figure denotes the PO_2 dependency of each resistance. In general, it is known that the dependency reflects the elementary reaction (or rate determining step, rds) of the ORR as described in the Appendix [28]. In Fig. 6, the PO_2 dependencies of R_1 and R_2 are ~0.08 and ~0.34, respectively, which correspond to the values controlled by the diffusion of O_{ad} along the BSCF surface to the TPB region and the charge transfer reaction (see Appendix). The dependence of R_3 was ~1.4, which is associated with oxygen molecular diffusion. Accordingly, in light of the electrical properties of the BSCF, cathode materials with enhanced cathodic performance could be developed by manipulating the surface oxygen ionic diffusion and charge transfer reaction kinetics.

In this study, Co_3O_4 and SNDC were added to BSCF and, as a result, improved performance was observed. This strategy is based on the following considerations: (1) the addition of Co_3O_4 enhances the electrical conductivity of BSCF; (2) SNDC has higher ionic conductivity than BSCF as seen in Fig. 3; and (3) composite cathodes reduce concerns regarding mechanical compatibility with SE and the particle growth of BSCF (note that the ceria (SNDC) has a lower TEC and higher melting temperature than BSCF).

Fig. 7(a) shows the impedance spectra of BSCF_cell, BC_cell, and BCS_cell at 600 °C in air. R_ps of the impedance spectra of BC_cell and BCS_cell decreased while the R_{ohmic}s values are similar to R_{ohmic} of BSCF_cell. In particular, R_p of BCS_cell is the lowest. This decreased R_p results from the enhanced kinetics of the surface oxygen ionic diffusion or the electronic charge transfer reaction, or both

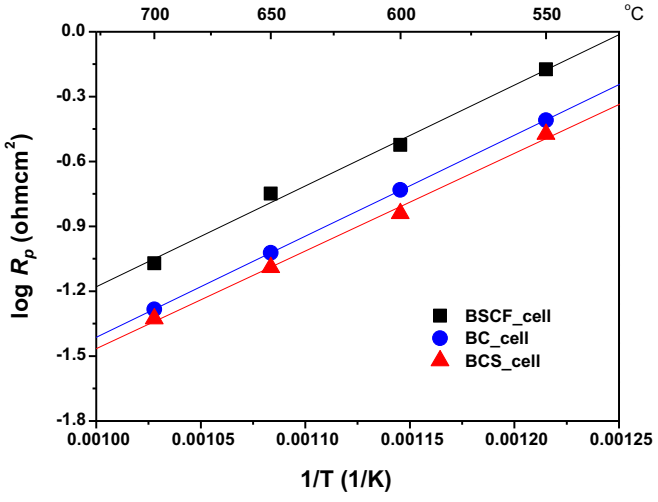

Fig. 8. Cathodic polarization resistances of BSCF_cell, BC_cell, and BCS_cell depending on temperature, respectively.

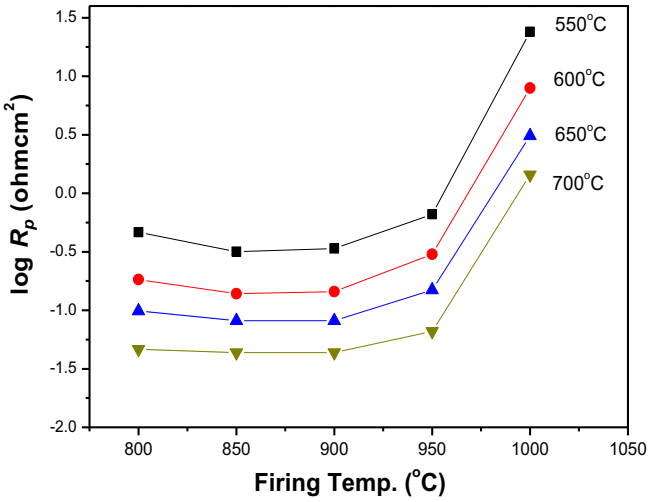

Fig. 9. Effect of cathodic firing temperature on R_p of BCS_cell.

corresponding to R_1 and R_2. This is verified by Bode plots of the cells. As seen in Fig. 7(b), BSCF_cell shows three peaks (f_{max}s: *a*, *b*, and *c*) while BC_cell and BCS_cell exhibit just two peaks (*a* and *c*). The second peak ($f_{max} = b$) of BSCF_cell corresponding to R_2 disappears in BC_cell and BCS_cell, indicating that the kinetics of the electronic charge transfer reaction is improved by Co_3O_4. The enhanced kinetics of the surface oxygen ionic diffusion by SNDC is indicated by the different height between the third peaks ($f_{max} = c$) of BCS_cell and other cells. The height of $f_{max} = c$ of BCS_cell corresponding to R_1 is slightly lower than those of BSCF_cell and BC_cell.

The Arrhenius plots of R_ps of BSCF_cell, BC_cell, and BCS_cell measured at different temperatures are shown in Fig. 8. As seen in this figure, R_ps and the activation energies of BC_cell and BCS_cell are lower than that of BSCF_cell (the activation energies of BSCF, BC, and BCS are estimated to be ~0.93 eV, 0.89 eV, and ~0.89 eV, respectively). Among them, BCS_cell shows the lowest R_p as expected. For instance, R_p of BCS_cell was measured to be ~0.048 Ω cm^2 at 700 °C. However, R_p of BCS_cell was highly affected by the cathode firing temperature.

Fig. 9 shows R_p as a function of the cathode firing temperature. As seen here, there was an optimal temperature region (850–900 °C). Lower or higher temperatures lead to increased R_p. The increased R_p at temperature lower than 850 °C may be attributed to insufficient adhesion between the cathode and the buffer layer or insufficient connectivity of the cathode particles. At temperature higher than 900 °C, it may be due to an increase of the particle size (note that the average particle size of BCS increases with temperature, as seen in Fig. 2(b)) and the existence of cobaltate (note that cobaltate was hardly detected at 1000 °C in XRD). A rapid increase of R_p was observed at 1000 °C firing.

3.5. *I–V and I–P tests*

An anode-supported tubular SOFC-cell with the BCS cathode was fabricated to investigate the high electrochemical performance of BCS. Fig. 10(a) shows its current–voltage (*I–V*) and current–power (*I–P*) characteristics. The inserted figure is a picture of the tubular cell investigated in this study. As noted earlier, the active area is quite large at 34.5 cm^2. For the electrochemical tests, ambient air

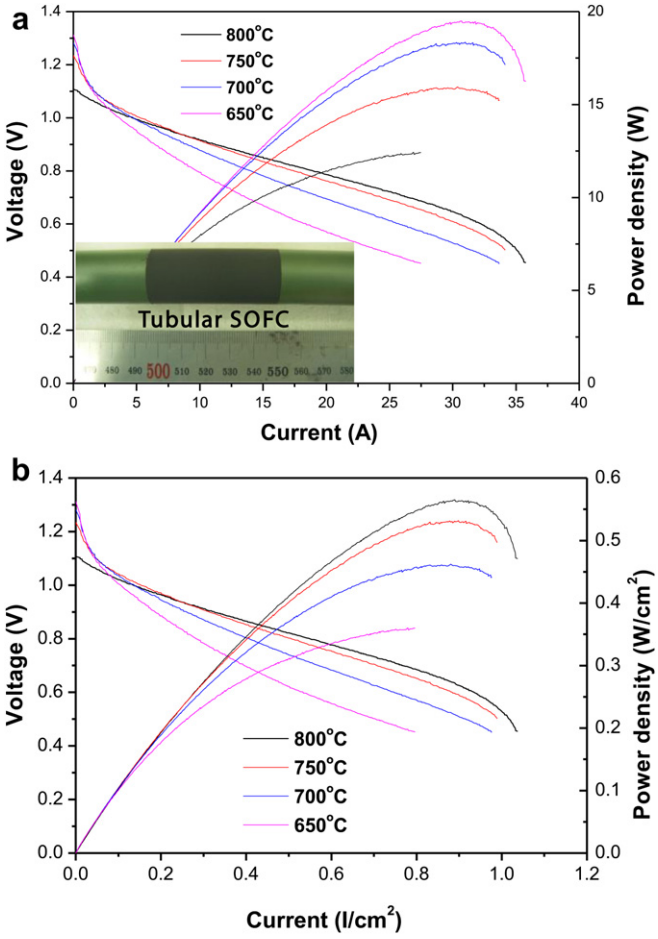

Fig. 10. (a) The dependencies of cell voltages and powers on current of the tubular cell with the BCS cathode (the inserted picture) at various temperatures between 650 °C and 800 °C. (b) The dependencies of cell voltages and power densities on current densities of the tubular cell.

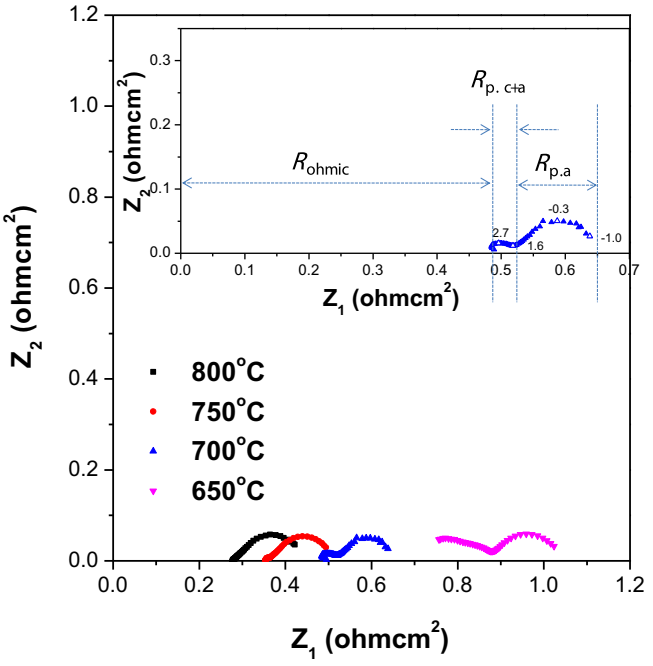

Fig. 11. Impedance spectra of the tubular cell with the BCS cathode at various temperatures. The inserted figure shows the enlarged impedance pattern obtained at 700 °C. $R_{p.a}$ is the anodic gas diffusion resistance of the cell and $R_{p.c+a}$ the cathodic and anodic polarization resistances.

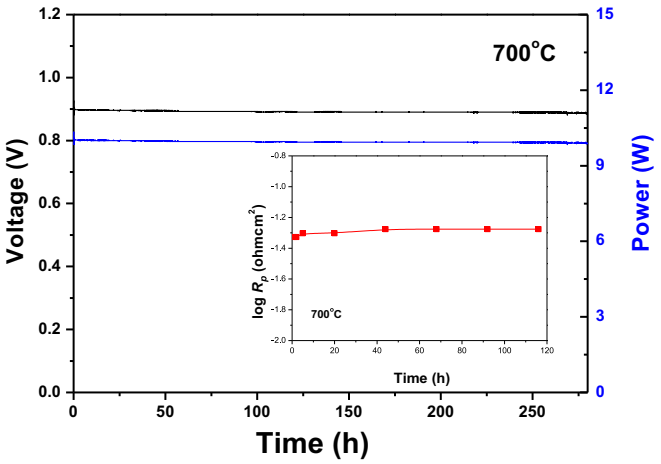

Fig. 12. The dependencies of cell voltage and power on time of the tubular cell. Applied cell current is 14 A and temperature is 700 °C. Flowing air was applied as the cathode atmosphere and hydrogen as the fuel. Inserted figure is the dependence of R_p on time of BCS_cell (symmetric cell) at 700 °C.

was applied as the cathode atmosphere and hydrogen as the fuel. The tests were carried out at various temperatures between 650 and 800 °C with a step of 50 °C. As seen in the figure, the OCV was slightly above 1.1 V, reflecting an almost perfectly sealed cell, and typical *I–V* and *I–P* curves were obtained. For instance, activated polarization loss of the cell was dominantly observed at low applied current range (<10 A) while concentration polarization loss was shown at a high applied current range (>30 A). Additionally, the cell performance decreased with decreasing operating temperature. Fig. 10(b) shows the power density of the cell as a function of current density. High performance was achieved. The power densities of the cell under 0.7 V at 800 °C, 750 °C, 700 °C, and 650 °C are 0.538 W cm^{-2}, 0.495 W cm^{-2}, 0.400 W cm^{-2}, and 0.277 W cm^{-2}, respectively. However, the obtained values are not as high as expected. This may be due to the high current collection resistance inherently occurring in large tubular cells (note that high current collection resistance is a feature of long tubular cells). To understand the origin of the cell resistances, EIS tests for the cell were conducted.

Fig. 11 exhibits the electrochemical impedance spectra of the tubular cell measured at various temperatures (650–800 °C). In the spectra, the high-frequency intercepts of the arcs to the *x*-axis correspond to R_{ohmic} and the sizes of the arcs indicate R_p, as analyzed in Fig. 4. As seen in this figure, R_{ohmic} is much higher than R_p. For example, R_{ohmic} is ~0.48 Ω cm^2 at 700 °C while R_p is 0.17 Ω cm^2 (see the inserted figure, which is an enlarged figure of the impedance pattern measured at 700 °C). Such high R_{ohmic} may be attributed to high current collection resistance, SE resistance, and the buffer layer resistance (note that cell performance highly depends on the current collection resistance in tubular SOFCs) [29–35]. In general, R_{ohmic} includes many types of ohmic resistances such as the SE resistance, the current collection resistance, the electrode ohmic resistance, and the contact resistance between each layer. However, it is unlikely that both the electrode ohmic resistance and the contact resistance highly affect R_{ohmic}, given the high electronic conductivity of the electrode and good adhesion between each layer. The activation energy (E_a) of R_{ohmic} is ~0.48 eV, which falls in the middle of the values of the ionic conduction of ScSZ (E_a ~ 0.8 eV)/GDC (E_a ~ 0.7 eV) and the current collection of a metal current collector (E_a is negligible). Thus, it is likely that R_{ohmic} is affected by both the SE/buffer layer resistances and the current collection resistance (note that the sum of the SE and buffer layer resistances estimated from their ionic conductivities in the tubular cell was ~0.1 Ω cm^2 at 700 °C (the thickness of the SE and buffer layer was about 15 μm)).

The impedance spectra related to R_p roughly consists of two semicircular arcs (this is clearly shown in the inserted figure). The first arc (high-frequency region, $R_{p,c+a}$) reduces with an increase of temperature while the second arc ($R_{p,a}$) shows little dependence on temperature. This indicates that the first arc is related to the activation process while the second arc is not. According to some reports [8,36], the second arc results from the concentration polarization resistance by the anode gas diffusion. In order to evaluate whether the second arc is dominantly affected by the anode gas diffusion, the impedance spectra under different anode gases from pure hydrogen to nitrogen were investigated. As a result, the second arc highly responds to the anode atmosphere while the first arc hardly changes (data not shown here). Additionally, this finding is supported by the measured frequency of the second arc. The log frequency corresponding to the second arc is below 1.6 (see the numbers in the inserted figure), which is a typical range corresponding to anode gas diffusion resistance [36]. The first arc corresponds to the sum of the polarization resistances of the cathode and anode ($R_{p,c+a}$). Barfod et al. reported that the arc obtained at a high-frequency range results from $R_{p,c+a}$ [36]. One interesting finding is that $R_{p,c+a}$ is ~0.06 Ω cm^2 at 700 °C, which is slightly higher than R_p (0.048 Ω cm^2) obtained from the symmetric cell (BCS_cell). Conclusively, R_p of the BCS on the zirconia SE system with the ceria buffer layer is extremely low (note that most of the resistance of the tubular cell originates from R_{ohmic} and $R_{p,a}$).

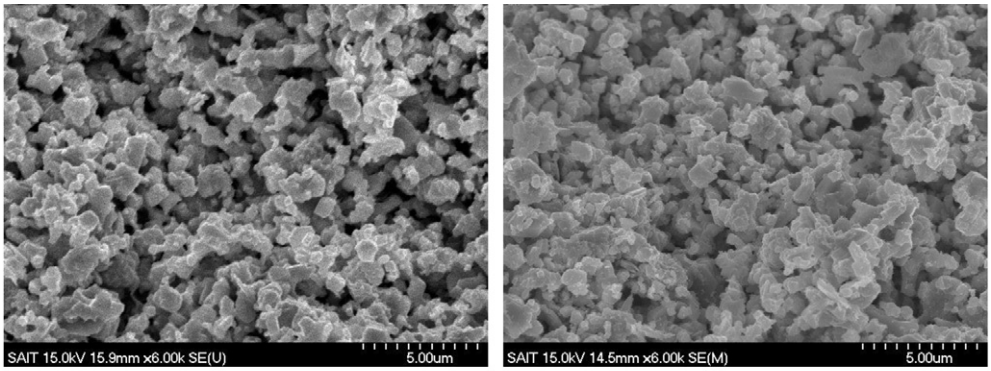

Fig. 13. SEM photographs of the BCS layers (a) before and (b) after the stability test of BCS_cell.

3.6. Durability

For the durability test of the tubular cell, the cell voltage and power were obtained under a galvanostatic condition by applying constant current of 14 A at 700 °C (the applying current corresponds to 0.8 V as seen in Fig. 10(a)). Flowing air was applied as the cathode atmosphere and hydrogen as the fuel. Fig. 12 presents the durability of the tubular cell. As seen in the figure, the cell performance was stable for 280 h, implying that all components of the cell were chemically and mechanically stable during the measurement. The stability of the cathode is confirmed from the symmetric cell (BCS_cell, the inserted figure). The symmetric cell test was carried out under flowing air. The inserted figure shows R_p depending on time in the symmetric cell. Stable R_p was observed for ~120 h.

Fig. 13 shows the microstructures of the BCS before and after the electrochemical test of the symmetric cell. As seen here, the microstructure after the test undergoes little deformation. Based on the SEM images, the average particle sizes and distributions (Fig. 14) were estimated from the Feret's mean diameter using an image analysis program (Matrox Inspector 2.1) [37,38]. The average particle sizes before and after the test were ~0.72 μm and ~0.74 μm, respectively, showing that the BCS is a reliable cathode material. The composite cathode is concluded to be a viable cathode for IT-SOFCs.

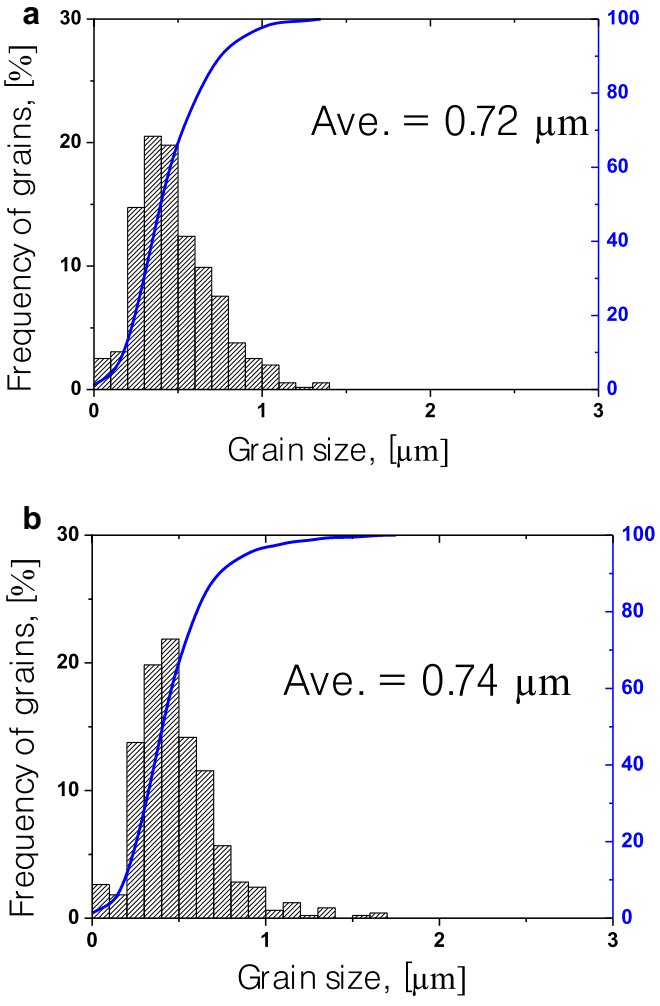

Fig. 14. The particle distributions of the BCS cathodes of (a) before and (b) after the stability test of BCS_cell.

4. Conclusions

We demonstrate a $Ba_{0.5}Sr_{0.5}Co_{0.8}Fe_{0.2}O_3 + Co_3O_4 + Ce_{0.8}Sm_{0.15}Nd_{0.05}O_2$ (0.72:0.08:0.20 in weight ratio) composite cathode having excellent electrochemical performance and high stability for IT-SOFCs. Its polarization resistance on a ScSZ solid electrolyte with a ceria buffer layer is ~0.048 Ω cm^2 at 700 °C, which is much lower than that of pure BSCF (0.085 Ω cm^2). This enhancement derives from enhanced mixed ionic and electronic conductivity by the addition of Co_3O_4 and $Ce_{0.8}Sm_{0.15}Nd_{0.05}O_2$. A large tubular SOFC-cell fabricated with the composite cathode shows good cell performance of 0.400 W cm^{-2} under 0.7 V and at 700 °C. Stable cell performance was observed during 280 h.

Acknowledgments

We would like to thank Dr. Han Wool Yu and Dr. Eun Soo Lee for supplying the tubular-cell test equipment.

Appendix

By use of Kroger–Vink notation, the overall oxygen reduction reaction (ORR) can be written as

$$1/2O_2 + V_o^{\cdot\cdot} + 2e \rightarrow O_o^x \quad (1)$$

where V denotes an oxygen vacancy and O_o^x oxygen ion in a normal oxygen site. The ORR consists of multiple elementary reactions as follows:

$$O_2(g) \rightarrow O_2(s) \quad \text{(step 1)}$$

$$O_2(s) \rightarrow 2O_{ad} \quad \text{(step 2)}$$

$$O_{ad} + e \rightarrow O_{ad}^- \quad \text{(step 3)}$$

$$O_{ad}^- \rightarrow O_{TPB}^- \quad \text{(step 4)}$$

$$O_{TPB}^- + e \rightarrow O_{TPB}^{2-} \quad \text{(step 5)}$$

$$O_{TPB}^{2-} + V_o^{\cdot\cdot} \rightarrow O_o^x \quad \text{(step 6)}$$

where *g*, *s*, and ad denote gas, surface, and adsorption. Here, different values of *n* in $R = R_o P O_2^{-1/n}$ indicate different elementary steps; for instance, $n = 1, 1/2, 3/8, 1/4$, and 0 reflects steps 1 (oxygen molecule diffusion), 2 (adsorption reaction), 3 (charge transfer reaction), 4 (surface oxygen ionic diffusion), and 6 (oxygen incorporation reaction), respectively [28].

References

[1] A.B. Stambouli, E. Traversa, Renew. Sust. Energy Rev. 6 (2002) 433–455.
[2] Z. Shao, C. Zhang, W. Wang, C. Su, W. Zhou, Z. Zhu, H.J. Park, C. Kwak, Angew. Chem. Int. Ed. 50 (2011) 1792–1797.
[3] J.R. Wilson, W. Kobsiriphat, R. Mendoza, H.Y. Chen, J.M. Hiller, D.J. Miller, K. Thornton, P.W. Voorhees, S.B. Adler, S.A. Barnett, Nat. Mater. 5 (2006) 541–544.
[4] W. Wang, C. Su, R. Ran, H.J. Park, C. Kwak, Z. Shao, Int. J. Hydrogen Energy 36 (2011) 5632–5643.
[5] Z. Shao, S. Haile, Nature 431 (2004) 170–173.
[6] W. Zhou, R. Ran, Z. Shao, J. Power Sources 192 (2009) 231–246.
[7] J. Molenda, K. Swierczek, W. Zajac, J. Power Sources 173 (2007) 657–670.
[8] M.J. Jorgensen, M. Mogensen, J. Electrochem. Soc. 148 (2001) A433–442.
[9] T. Suzuki, M. Awano, P. Jasinski, V. Petrovsky, H.U. Anderson, Solid State Ionics 177 (2006) 2071–2074.
[10] S.P. Jiang, J. Mater. Sci. 43 (2008) 6799–6833.
[11] W.K. Hong, G.M. Choi, J. Membr. Sci. 346 (2010) 353–360.
[12] J. Gao, X. Liu, D. Peng, G. Meng, Catal. Today 82 (2003) 207–211.

[13] W.H. Kim, H.S. Song, J.H. Moon, H.W. Lee, Solid State Ionics 177 (2006) 3211–3216.
[14] D. Chen, C. Huang, R. Ran, H.J. Park, C. Kwak, Z. Shao, Electrochem. Commun. 13 (2011) 197–200.
[15] H. Zhang, H. Liu, Y. Cong, W. Yang, J. Power Sources 185 (2008) 129–135.
[16] Z. Shao, G.X. Xiong, J.H. Tong, H. Dong, W.S. Yang, Sep. Purif. Technol. 25 (2001) 419–429.
[17] S. Lee, H.S. Song, S.H. Hyun, J.S. Kim, J.H. Moon, J. Power Sources 187 (2009) 74–79.
[18] Z. Duan, M. Yang, A. Yan, Z. Hou, Y. Dong, Y. Chong, M. Cheng, W. Yang, J. Power Sources 160 (2006) 57–64.
[19] W.X. Kao, M.C. Lee, T.N. Lin, C.H. Wang, Y.C. Chang, J. Power Sources 195 (2010) 2220–2223.
[20] Q. Zhu, T. Jin, Y. Wang, Solid State Ionics 177 (2006) 1199–1204.
[21] H. Wang, W.S. Yang, Y. Cong, X. Zhu, Y.S. Lin, J. Membr. Sci. 224 (2003) 107–115.
[22] S. Mclntosh, J.F. Vente, W.G. Haije, D.A. Blank, H.J.M. Bouwmeester, Chem. Mater. 18 (2006) 2187–2193.
[23] H.J. Park, S. Kim, Electrochem. Solid-State Lett. 10 (2007) B187–190.
[24] V. Dusastre, J.A. Kilner, Solid State Ionics 126 (1999) 163–174.
[25] E.P. Murray, S.A. Barnett, Solid State Ionics 143 (2001) 265–273.
[26] E. Bucher, A. Egger, P. Ried, W. Sitte, Solid State Ionics 179 (2008) 1032–1035.
[27] H.J. Park, S. Kim, J. Phys. Chem. C 111 (2007) 14903–14910.
[28] Y. Zheng, R. Ran, Z. Shao, J. Phys. Chem. C 112 (2008) 18690–18700.
[29] O. Yamamoto, Y. Arati, Y. Takeda, N. Imanishi, Y. Mizutani, M. Kawai, Y. Nakamura, Solid State Ionics 79 (1995) 137–142.
[30] Y.J. Kang, H.J. Park, G.M. Choi, Solid State Ionics 179 (2008) 1602–1605.
[31] H. Zhu, R.J. Kee, J. Power Sources 169 (2007) 315–352.
[32] Y. Bai, C. Wang, C. Jin, J. Liu, Fuel Cells 11 (2011) 465–468.
[33] C. Hatchwell, N.M. Sammes, I.W.M. Brown, K. Kendall, J. Power Sources 77 (1999) 64–68.
[34] T. Suzuki, T. Yamaguchi, Y. Fukishiro, M. Awano, J. Power Sources 163 (2007) 737–742.
[35] C. Jin, J. Liu, L. Li, Y. Bai, J. Membr. Sci. 341 (2009) 233–237.
[36] R. Barfod, M. Mogensen, T. Klemenso, A. Hagen, Y.L. Liu, P.V. Hendriksen, J. Electrochem. Soc. 154 (2007) B371–378.
[37] H. Moon, B.K. Kim, S.J.L. Kang, Acta Mater. 49 (2001) 1293–1299.
[38] Y.I. Jung, S.Y. Choi, S.J.L. Kang, Acta Mater. 54 (2006) 2849–2855.